

Article

Microparticle Inertial Focusing in an Asymmetric Curved Microchannel

Arzu Özbey¹, Mehrdad Karimzadehkhoei¹ , Hossein Alijani¹ and Ali Koşar^{1,2,*} 

¹ Mechatronics Engineering Program, Faculty of Engineering and Natural Sciences, Sabanci University, Tuzla, Istanbul 34956, Turkey; ozbeyarzu@sabanciuniv.edu (A.Ö.); mehrdad@sabanciuniv.edu (M.K.); hossein@sabanciuniv.edu (H.A.)

² Center of Excellence for Functional Surfaces and Interfaces for Nano-Diagnostics (EFSUN), Sabanci University SUNUM Nanotechnology Research Center, Sabanci University, Tuzla, Istanbul 34956, Turkey

* Correspondence: kosara@sabanciuniv.edu; Tel.: +90-216-483-9621

Received: 30 July 2018; Accepted: 7 August 2018; Published: 9 August 2018



Abstract: Inertial Microfluidics offer a high throughput, label-free, easy to design, and cost-effective solutions, and are a promising technique based on hydrodynamic forces (passive techniques) instead of external ones, which can be employed in the lab-on-a-chip and micro-total-analysis-systems for the focusing, manipulation, and separation of microparticles in chemical and biomedical applications. The current study focuses on the focusing behavior of the microparticles in an asymmetric curvilinear microchannel with curvature angle of 280°. For this purpose, the focusing behavior of the microparticles with three different diameters, representing cells with different sizes in the microchannel, was experimentally studied at flow rates from 400 to 2700 $\mu\text{L}/\text{min}$. In this regard, the width and position of the focusing band are carefully recorded for all of the particles in all of the flow rates. Moreover, the distance between the binary combinations of the microparticles is reported for each flow rate, along with the Reynolds number corresponding to the largest distances. Furthermore, the results of this study are compared with those of the microchannel with the same curvature angle but having a symmetric geometry. The microchannel proposed in this study can be used or further modified for cell separation applications.

Keywords: microfluidics; inertial focusing; fluorescent particle focusing; curvilinear microchannel

1. Introduction

The rapid advances in Microfluidics and Nanofluidics fields have led to compact microfluidic devices and emerging cell applications that offer potential benefits in providing lab-on-a-chip (LOC) platforms for disease diagnosis and treatment [1–7]. Thanks to the progress in micro/nano fabrication techniques, the microfluidic applications in various subjects, such as DNA analysis [1–3], cytometry [4,5], micromixing [6], microreactors [7], cell cycle synchronization [8], drug delivery [9] and extraction of blood plasma [10], have appeared over the past decades. One of the distinct advantages of the microfluidic systems is their capability to be integrated into other systems. In particular, the use of LOC platforms allowed the combination of several methods within a single device [11]. For instance, the micro-total-analysis systems (μTAS) were designed by combining different applications/components, such as cytometers, bioreactors, and the separation into a single system [12]. Such an integrated system covering a small area requires very low amounts of fluids from microliter (10^{-6} L) down to attoliter (10^{-18} L), depending on the application and scale during its operation [8,10–13].

The particle separation and detection of some cells or biomolecules is one of the most studied topics in this area. Active or passive methods are the major categories of separation techniques [14,15].

While the former utilizes external forces [16,17], such as magnetic [18], dielectric [19] or acoustic [20] force, the latter relies on channel geometry and internal forces. Passive separation methods mainly exploit hydrodynamic forces in microscale, and heavily depend on surface properties of the microchannel geometry. Furthermore, as fabricating the passive separation devices is cost effective and less complicated than the active ones, integrating them into a lab-on-a-chip device is also much simpler.

The passive techniques for particle or cell separation/focusing include [21] inertial focusing, pinched flow [22] and hydrodynamic spreading [23], deterministic lateral displacement [24], hydrophoretic filtration [25], size exclusion filtration [26], cross-flow filtration [27], and hydrodynamic filtration [28]. Specifically, the most common microchannel configurations utilizing the inertial forces with the help of their geometry, include straight [29–37], straight with contraction and expansion regions [10,38–43], and curvilinear channels including spiral [44–51] and serpentine [52–55] channels. Depending on the balance of the hydrodynamic forces acting on microparticles or cells, they pass along specific paths in the flow direction, known as the focusing (focal or equilibrium) position. In inertial microfluidics, the acting forces are the functions of the microchannel geometry, fluid properties, microparticles dimensions, shape, and deformability. Additionally, the particle–particle interactions (for high particle concentration) [56,57] or fluid–particle interactions [58] should be taken into account when interpreting the results. In the straight channels, the particle Reynolds number and confinement ratio of the microchannel are the two major parameters determining the focal position of the microparticles. For instance, the microparticles flowing at moderate Reynolds numbers inside a straight microchannel with a square cross section focus at four equilibrium locations at the center of the walls; while in the low aspect ratio rectangular cross sections, the microparticles focus along the center of the two long edges [35].

Curved geometries induce secondary flows, especially in the regions with a fading lateral force. Therefore, introducing curvilinearity to a microchannel with rectangular cross section yields that are in better control of the number and position of the equilibrium positions. In other words, handling the focal positions is easier in curved microchannels [59–61]. In the curvilinear microchannels, the velocity of the fluid passing along the centerline differs from that of the fluid passing near the walls. Consequently, the inertia is increased near the centerline. Thus, a pressure gradient in the radial direction is generated; consequently, the fluid near the inner wall and the fluid near the outer wall tend to move outward and inward, respectively (both in a transverse direction). Therefore, two symmetric vortices, which introduce the Dean drag force (F_D) to the system, form [59,61].

Spiral [51] and curved serpentine [62] microchannels are the two main categories of curvilinearity. Particularly, the designs of curvilinear serpentine channels include symmetric [62,63] and asymmetric [53,64,65] geometries. Recently, various studies on such geometries were conducted in the literature. For example, Di Carlo et al. studied the inertial focusing of microparticles with a diameter of 9 μm at particle Reynolds numbers up to 2.9 using three different geometries [62]. While the microparticles focused along four streams in a straight microchannel with a square cross-section, a symmetric geometry reduced the number of focusing positions to two, and an asymmetric geometry further reduced the focusing positions to a single streak. It is worth mentioning that the curvature angle of the symmetric and asymmetric microchannels was 180° . In another study, an asymmetrically curved microchannel was used to separate and filter the particles with different sizes only with hydrodynamic forces [64]. At the flow rate of 900 $\mu\text{L}/\text{min}$, 9- μm -diameter microparticles focused along a single stream at the outlet of the channel, while small particles of a 3.1 μm diameter remained unfocused and distributed over the entire outlet width. The underlying physics of the particle focusing in the curved microchannels was further investigated in a series of asymmetric curved microchannels, under different flow conditions [65]. Accordingly, the focusing of microparticles occurred at channel Reynolds number of 270, in a channel with a varying width.

In this study, focusing the behavior of polystyrene microparticles in an asymmetric curvilinear microchannel with curvature angle of 280° was experimentally studied. To do so, particles of a 10, 15, and 20 μm diameter were pumped into the microchannel, with flow rates between 400 and

2700 $\mu\text{L}/\text{min}$, corresponding to the Reynolds number range of 30–205. At each Reynolds number, the focusing position and width of each particle were measured and reported in two particular regions; the transition region, which is the inflection point of the last two curves of the microchannel, and the outlet region. Moreover, for each binary combination of the particles, the optimum Reynolds number, defined as the one at which the largest distance between the focal bands of two particles at the transition region occurs, was reported. Lastly, the focusing behavior of the particles in the current asymmetric microchannel was compared to the symmetric design with the same curvature angle, which was previously done in our group [63]. An asymmetric microchannel configuration with such a high curvature angle and the comparison of its performance with the corresponding symmetric design over a wide range of Reynolds number, constitutes the significance of this study.

2. Theoretical Background

Understanding the forces acting on microparticles or cells plays an important role in accurately predicting their focal positions. The main forces that are applied on the microparticles in the microchannels include shear gradient lift force (F_S) and wall induced lift force (F_W). In curved microchannels, additionally, F_D exists because of the formation of the secondary flow. It should be mentioned that all of these forces are in a transverse direction (Figure 1b).

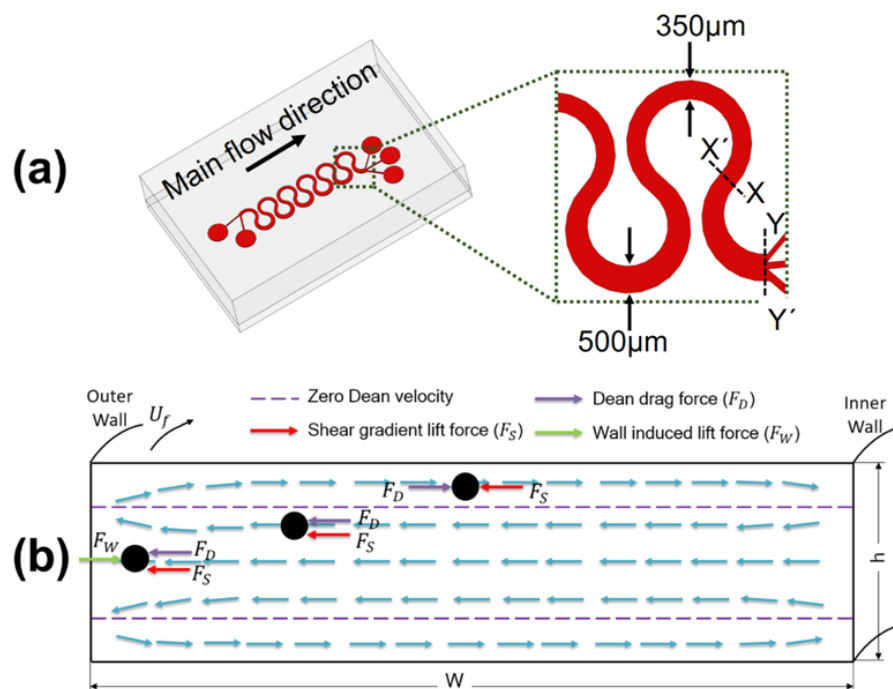


Figure 1. (a) Drawing of the asymmetric microchannel and a zoom-in view of the transition region (X–X', 350 μm in width) and the outlet region (Y–Y', 500 μm in width). (b) The direction of the secondary flow vortices and forces applying on a particle (according to its location in the cross section) at typical positions in the curvilinear microchannel.

For a microparticle in fluid flow, because of the parabolic velocity profile of the Poiseuille flow, its upper side has a larger relative velocity (in magnitude) than its lower side. This reduces the pressure on the upper side of the particle and, consequently, F_S is generated, by which the particle is pushed away from the centerline, towards the channel walls, until this force is balanced by F_W [66,67]. In other words, a particle tends to follow the path along which its sides undergo a minimum difference in relative velocity. The magnitude of F_S is given as follows:

$$F_S = C_L \frac{\rho U_{max}^2 a^3}{D_h} \quad (1)$$

where C_L is the lift coefficient, ρ is the fluid density, U_{max} is the maximum velocity of the fluid, a is the diameter of the microparticle, and D_h is the channel hydraulic diameter. Accordingly, F_S is strongly affected by the position and diameter of the particle and fluid velocity, while it is independent of the particle rotation [68,69].

In addition, there are two main reasons for F_W [70,71]. When a particle moves near a wall of the channel, the wall breaks the axisymmetry of the wake vorticity distribution, which is generated at the particle's surface. As a result, an induced velocity emerges, further breaks the symmetry, and generates F_W that repels the particle. Moreover, the presence of the walls makes the particle move with a velocity somewhat smaller than that of the fluid [60,68]. Secondly, because of the particle-flow interaction, flow streamlines are deviated towards the sides of the particle, and the relative fluid velocity is accelerated on the upper part of the particle, thereby creating a low pressure on this side. Therefore, the particle is repelled away from the wall by F_W . It is worth mentioning that the magnitude of this force increases as the distance between the particle and the wall decreases. F_W is expressed as follows:

$$F_W = C_W \frac{\rho U_{max}^2 a^6}{D_h^4} \quad (2)$$

where C_W is the lift coefficient, which depends on the position of the particle in the channel and the Reynolds number of the fluid [68,69]. Notably, the two aforementioned lift forces have opposite directions when applying on a microparticle.

Moreover, the net inertial lift force (F_L) is calculated by the following formula:

$$F_L = C_L \frac{4\rho U_f^2 a^4}{D_h^2} \quad (3)$$

where U_f is the mean flow velocity. The lift coefficient (C_L) depends on the channel Reynolds number (Re_c) and the location of the particle in the channel. For the case of Re_c lower than one hundred, C_L is approximated to 0.5 [47,72]. In addition, the F_L has an inverse relationship with the Reynolds number [61].

When F_S and F_W are in balance, according to the tubular pinch effect, the particles may focus along an equilibrium position. The successful focusing of the particles occurs when the magnitude of the particle diameter over the channel hydraulic diameter ($\lambda = a/D_h$) is greater than 0.07 for $Re_p > 1$ [62], where Re_p (the particle Reynolds number) is calculated by the following formula:

$$Re_p = Re_c \left(\frac{a}{D_h} \right)^2 \quad (4)$$

The particle focusing positions can be further controlled by using curved geometries [59,61]. As mentioned previously, in curved microchannels, the inertia force is higher in magnitude in the centerline. On one hand, the fluid passing along the centerline generates a pressure gradient by flowing outwards. The resultant centrifugal pressure gradient, on the other hand, makes the fluid in the proximity of the outer wall flow inwards. This results in the formation of two symmetric vortices in a curved microchannel, the so-called secondary flow that exerts F_D on the particle, whose magnitude is calculated through the following formula [50]:

$$F_D = 3\pi\mu U_{De} a \quad (5)$$

where the viscosity of the fluid is denoted by μ , and U_{De} is the average Dean velocity, defined as follows:

$$U_{De} = 1.8 \times 10^{-4} D_e^{1.63} \quad (6)$$

In this formula, De is the dimensionless Dean number, given as follows:

$$De = \frac{\rho U_f D_h}{\mu} \sqrt{\frac{D_h}{2R}} = Re_c \sqrt{\frac{D_h}{2R}} \quad (7)$$

where R is channel curvature radius [61].

Overall, in the curved microchannels, the particles focus in a location, where all of the above-mentioned forces constitute an equilibrium.

3. Materials and Methods

3.1. Microchannel Fabrication

The microchannel was made of polydimethylsiloxane (PDMS) using the standard soft lithography fabrication techniques. The following steps were followed to fabricate the chip: (a) spinning SU-8 3050 photoresist (Microchem Corp., Westborough, MA, USA) on the polished side of a 3" silicon wafer, using a spinner (SPS Europe, SPS-Europe GmbH, Ingolstadt, Germany); (b) soft baking the photoresist layer, followed by the UV exposure of the photoresist with a Mask Aligner UV-lithography device (MDA-60MS, Midas System Co., Ltd., Daejeon, South Korea) through an image reversal acetate mask containing printed geometry of the microchannel printed with 10,000 DPI (Dots Per Inch) resolution (by CAD/Art Services, Inc., Bandon, OR, USA); (c) after hard bake, developing unexposed parts of the photoresist by SU-8 Developer (Microchem Corp., Westborough, MA, USA); (d) pouring a well-mixed mixture of 10 to 1 (weight to weight) ratio of PDMS prepolymer (Sylgard 184 silicone elastomer kit, Dow Corning, Midland, MI, USA) to curing agent (Sylgard 184 silicone elastomer kit, Dow Corning, Midland, MI, USA) over the silicon master contained in a glass petri dish; (e) 1-h degassing of PDMS in a vacuum oven (Cole-Parmer, Lake Forest, IL, USA) under low pressure (76 mmTorr) to eliminate the trapped air bubbles, followed by curing for 12 h at 75 °C; (f) peeling off the PDMS from the silicon master and cutting it using a bladed instrument; (g) punching holes for the inlet and outlets by a 21-gauge needle; (h) cleaning both pieces with Isopropyl alcohol (IPA) and deionized (DI) water and drying by Nitrogen blow, bonding the PDMS to a microscopic glass slide by an oxygen plasma bonding device (Harrick Plasma Cleaner, Ithaca, NY, USA), activating for 60 s; and (i) resting the PDMS chip on a hotplate (Dorutek, Ankara, Turkey) at 75 °C for 15 min to make the bond stronger.

3.2. Particle Suspensions

Neutrally buoyant fluorescent polystyrene microparticles with diameters of 20 μm (Phosphorex, Holliston, MA, USA), 15 μm (Invitrogen, Carlsbad, CA, USA), and 10 μm (Invitrogen, Carlsbad, CA, USA) were employed in the focusing experiments. In this context, they are called 'small', 'medium', and 'large' particles, respectively. To decrease the particle–particle interaction, a low particle concentration was used. For this purpose, weight fraction of the microparticles was fixed at 0.01%, and the solution (with an initial 1% weight concentration) was diluted with DI water.

3.3. Experimentation

The suspension of each particle was loaded to a 50 mL plastic syringe and pumped into the microchannel by a syringe pump (PHD 2000, Harvard Apparatus, Holliston, MA, USA) with flow rates varying from 400 μL/min to 2700 μL/min with 100 μL/min increments. Each test corresponding to a flow rate lasted for 90 s. TYGON tubing (LMT-55, IDEX Corp., Harbor, WA, USA, internal diameter: 250 μm, length: 150 mm) and the appropriate fittings (IDEX Corp., Harbor, WA, USA) were used for connecting the tip of the syringe to the inlet of the chip and the outlet of the chip to the outlet reservoir. Each experiment was performed three times. The results were consistent in all of the three times.

3.4. Fluorescent Imaging and Data Analysis

An inverted phase contrast microscope (IX72, Olympus, Tokyo, Japan), having a (12-bit) charge coupled camera (DP 72, Olympus, Tokyo, Japan) and mercury lamp (U-LH100HG, Olympus, Tokyo, Japan) with a 600 ms exposure time was used to take videos of the particles' flow at the transition and outlet regions. For all of the particles, the video of each flow rate was processed as follows: (a) separation of videos to approximately 60 stacks using ImageJ software; (b) overlaying all of the stacked images to have the complete and smooth fluorescent streams; (c) drawing two lines on X–X' (transition) and Y–Y' (outlet) sections and exporting the fluorescent intensity along them, with the line intensity module of the ImageJ software; (d) using the ImageJ plotting line profile module to measure the focusing position and focusing width of the particles streams; (e) implementing each line scan data in the OriginPro-2015 Software to achieve a representative column of pixels in the Reynolds maps. ImageJ software was used for coloring the superimposed images. Further details can be found in the literature [73].

4. Results and Discussion

The geometry of the asymmetric curvilinear microchannel is depicted in Figure 1a. It is a repeated pattern of two different curves, namely: (1) 280-degree curves of a uniform width of 350 μm followed by (2) 280-degree curves with varying width from 350 μm to 500 μm . There are 11 inflection points in total. The height of the microchannel is 90 μm . Although originally two inlets were considered for the microchannel, and in current work the particles flow through one inlet only. Moreover, the Reynolds numbers reported in this study were calculated at the beginning of the inlet, where the microchannel has uniform width of 350 μm .

As a secondary flow in the curvilinear microchannel exists, the particles move in a transverse direction (relative to the main fluid flow). To appropriately investigate the particle motion, it is preferred to consider the particles' position in two specific cross sections, transition region and outlet region, as depicted in Figure 1a. Because of the presence of an inflection point at the transition region, and in order to avoid further confusion, the wall between X and Y is labelled as W_2 , and the one between X' and Y' is labelled as W_1 .

The mean velocity profile has a major effect on the movement of microparticles in microchannels. It is noteworthy that in straight microchannels, the fluid flow has a three-dimensional (3D) parabolic velocity profile. Its maximum is located at the center point of the channel cross section and its zero values are present on the walls. Accordingly, at each cross section, F_S acts on the particles from the center point towards the walls. The magnitude of this force at the centerline is zero. For the case of curved channels, the maximum of the velocity does not occur at the centerline of the microchannel because of the presence of secondary flow (Dean flow) [61]. The Dean flow consists of two counter-rotating vortices in transverse direction. At the mid-height of the channel, the secondary flow directs towards the outer wall. In addition, two zero Dean velocity lines exist between the centerline and the upper and lower walls of the microchannel (closer to the walls). Between each of these lines and their corresponding wall, the secondary flow directs towards the inner wall. Between the two zero Dean velocity lines, its direction is the other way around (Figure 1b). Additionally, in the microfluidics studies involving particle or cell separation in a spiral geometry, this pattern is preserved up to a specific Dean number [47]. According to some numerical studies, the main flow velocity has a maximum somewhere between the centerline and the inner wall [63,74]. F_L is always directed from the velocity maxima towards the channel walls, regardless of the particle vertical position. When the particles are near the outer wall, the direction of F_L is the same as that of F_D towards the outer wall. Thus, the particles migrate transversally along the rotational direction of the secondary vortices. When the particles are near the inner wall, F_L balances F_D . Hence, in spiral microchannels, the particle stream focuses near the inner wall.

For an alternating curvilinear geometry, any change in the curvature yields in a change in the directions of the secondary flow and the case becomes more sophisticated compared to spiral

microchannels. Therefore, it is a challenging task to accurately anticipate the steady state condition of the Dean vortices. It has been demonstrated in our previous work, that in a symmetric curvilinear microchannel with a uniform width of 350 μm and a curvature angle of 280° , when the fluid flow approaches the transition region, a shift in the velocity maxima is observed near the centerline of the channel [63]. Thereafter, the outer wall becomes the inner wall and the velocity maxima occurs closer to the inner wall, rather than to the centerline. This is in a general agreement with a similar study on asymmetric curvilinear microchannels [62]. Hence, F_5 changes in both horizontal and vertical directions because of these continuous shifts in the velocity maxima in the cross section. The particles' focal positions and widths are plotted in Figure 2 as a function of the Reynolds numbers.

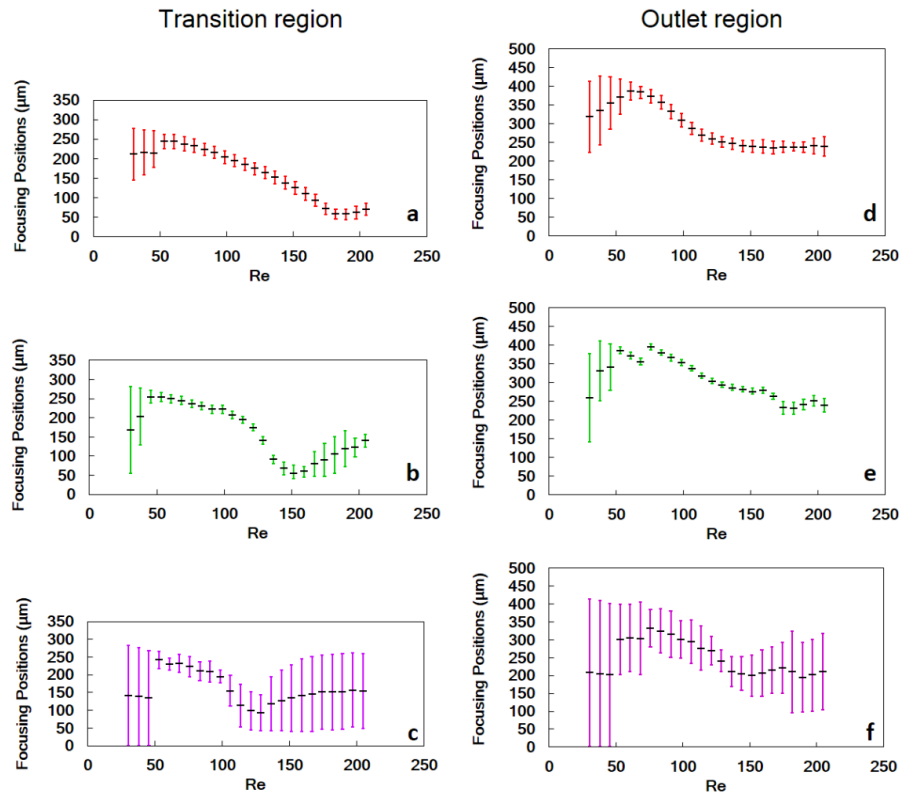


Figure 2. Focusing position against the Reynolds numbers (Re) at the transition region for the particles of (a) 20 μm , (b) 15 μm , and (c) 10 μm diameter as well as at the outlet region for the particles of (d) 20 μm , (e) 15 μm , and (f) 10 μm diameter. The width of the focusing bands is shown by error bars. The focal positions of 0 and 350 μm in (a–c) correspond to walls W_2 and W_1 , and 0 and 500 μm in (d–f) represent inner and outer walls, respectively.

4.1. Large Particles

At low Reynolds numbers ($Re \sim 30$) and in the transition region, the focusing position of large particles ($a = 20 \mu\text{m}$, $\lambda_1 = 0.139$, and $\lambda_2 = 0.129$) is deviated from the centerline slightly towards W_1 , spreading over a band, which has a width of approximately seven times as big as the diameter of a single particle (Figures 2a and 3a). This is because of the insignificant magnitudes of the flow velocity as well as F_L and F_D . As the particles pass along the outlet region, the band is widened by a factor of around 1.5 (Figures 2d and 3d), as F_D increases and F_5 decreases. When Re is approximately 53, a particle streak, with a width twice as big as a single particle's diameter, forms in the transition region. Similar to the lower Re , the streak is deviated from the centerline slightly towards W_1 . At this Re , the particle focusing width in the outlet region is larger. Although the focusing width becomes smaller compared to the lower Re values, it is still about five times bigger than the diameter of a single

particle. This wide stream is still closer to W_1 at the transition region and to the outer wall in the outlet region. It can be claimed that the ratio of F_L/F_D is higher in the transition region, because the channel hydraulic diameter D_h is smaller in this region (143 μm versus 152 μm for the outlet region). In the outlet region F_S acts on the particle towards the outer wall, whilst F_D has an opposite direction. This is because of the assumption for the particles to be between zero Dean velocity lines and their corresponding wall. When a particle approaches the transition region, F_S increases and F_D decreases, leading to a tighter particle focusing stream. On the other hand, when a particle approaches to the outlet region, F_S decreases and F_D increases. Because of the mixing effect of Dean vortices, the single particle stream at the transition region widens when reaching the outlet region. However, both F_S and F_D increase with main flow velocity ($F_L \propto U_f^2$, $F_D \propto U_f^{1.63}$). Therefore, at $Re \sim 53$, large particles focus as a relatively tight stream in both the transition and outlet regions. Although the lift coefficient (C_L) decreases with the flow velocity, the increase in F_S is still greater than that in F_D ($F_S \propto a^3$, $F_D \propto a$). Consequently, the particle stream is closer to W_2 in the transition region and moves towards the inner wall in the outlet region. When $Re > 172$, the particles' stream approaches W_2 in the transition region and is repelled by the F_W of this wall. At the same time, the particles are pushed away from the velocity maxima towards W_2 . It is worth mentioning that, as a result of the curvilinear geometry and aforementioned lift and drag forces, the particles do not follow the essential flow streamlines, and rather, they migrate perpendicular to them as they approach the outer wall or W_2 . Moreover, the focusing width remains unchanged for $53 \leq Re \leq 205$ and $68 \leq Re \leq 189$ in the transition (Figure 2a,d) and outlet regions (Figure 3a,d), respectively.

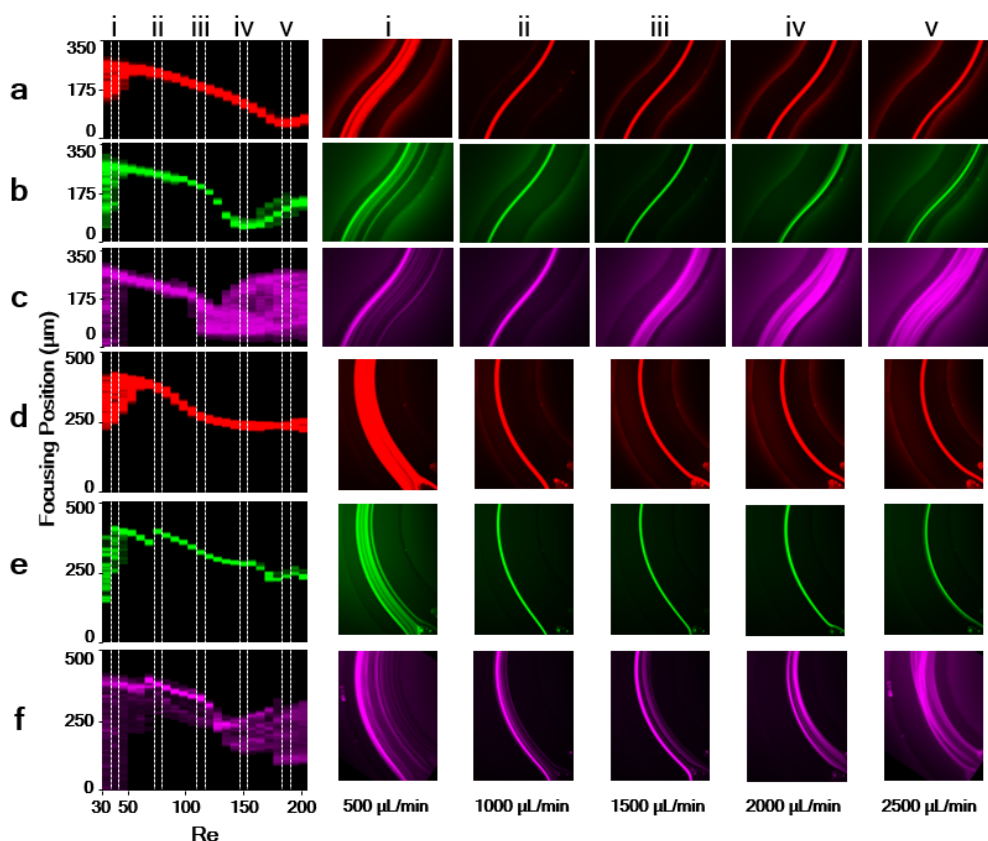


Figure 3. *Re* maps of the asymmetric curvilinear microchannel in the transition region for microparticles of (a) 20 μm , (b) 15 μm , and (c) 10 μm diameter, and in the outlet region for the microparticles of (d) 20 μm , (e) 15 μm , and (f) 10 μm diameter. (i–v) Real images of the particles flow at the five rates indicated (main flow direction is downward in all the images).

4.2. Medium Particles

At low Reynolds numbers ($Re \sim 30$) and in the outlet region, medium particles ($a = 15 \mu\text{m}$, $\lambda_1 = 0.1$, $\lambda_2 = 0.09$) cover half of the width of the microchannel at the centerline, while they do not focus at the transition region. This is because at low flow velocities, the magnitudes of F_S and F_D are not high enough to influence the particles. With increasing Re to 45, the particles focus in a band with a width of approximately two times the size of a single particle's diameter in the middle of the distance between the centerline and wall W_1 in the transition region (Figures 2b and 3b). However, such a tight stream is not observed in the outlet region for the same Re (Figures 2e and 3e). The focusing behavior of the medium particles is similar to that of the large particles; as they approach the outlet region, F_D increases and F_S decreases as a result of increasing D_h . By increasing the Reynolds number, the single particle stream gradually moves away from W_1 . Because both the horizontal and vertical components of the F_S scale with a^3 and F_D with a , large particles are pushed towards the top and bottom channel walls less than medium size particles at the same flow rate, and they tend to focus near the zero Dean velocity lines. The vertical position of medium particles seems to be between the upper and lower zero Dean velocity lines when they start the transverse motion. In this case, although the direction of F_S remains the same (towards W_2), the direction of F_D becomes from W_2 towards the centerline in the transition region. Since a strong reciprocal relationship exists between the lift coefficient and the main flow velocity [72], as the flow velocity increases, the F_L declines in both horizontal and vertical directions. Consequently, the medium particles tend to move to half-height of the microchannel, where the Dean flow directs towards the outer wall. Here, the directions of F_S and F_D are towards the outer wall in the outlet region. Therefore, moving from the transition region to the outlet region, the stream of particles gradually migrates from W_2 to the centerline. Moreover, above $Re \sim 144$, the particles start to lose their focusing trend in the transition region.

4.3. Small Particles

For the Reynolds numbers below 50, the small particles ($a = 10 \mu\text{m}$, $\lambda_1 = 0.069$, $\lambda_2 = 0.064$) focus neither in the transition region (Figures 2c and 3c) nor in the outlet region (Figures 2f and 3f). For $53 \leq Re \leq 106$, they tend to focus in the transition region as a wide band (compared to the diameter of single particles) closer to W_1 in the transition region, and the outer wall in the outlet region, similar to large and medium particles. At this Reynolds number range, the particle vertical position is assumed to be between the zero Dean velocity lines and their corresponding walls, closer to the zero Dean velocity line compared to the large and medium size particles. At the upstream location of the transition section, F_S acts on the particles towards the outer wall, as a balancing force of F_D . Because of the higher hydraulic diameter, F_S is smaller and F_D is larger in this region. Therefore, the focused particle stream is seen near W_1 at the transition region. Similarly, in the downstream location of the transition region, F_D increases so that mixing effect of the F_D results in a wider focusing band in the outlet region. However, the focusing band migrates towards the centerline with an increase in the flow velocity, which is a stronger function of F_S compared to F_D ($F_S \propto U_f^2$, $F_D \propto U_f^{1.63}$). In the transition region, increasing Re beyond 106 results in a sudden defocusing behavior, which is probably because the vertical position of small particles approaches the half-height of the channel, where the direction of F_D is reversed. F_D and F_S have identical directions (towards W_2 in the transition and the outer wall in the outlet region). Therefore, in the transition region, the particles approach W_2 by increasing Re to 129. Increasing the flow rate causes a mixing effect on the microparticles because, as mentioned before, the lift coefficient decreases with the flow velocity and, at some point, F_S becomes smaller than F_D . Furthermore, although the previous studies claimed that the lowest limit of the particle diameter to channel hydraulic ratio ($\lambda = a/D_h$) is 0.07 for successful particle focusing, the small particles still focus in a relatively wide band (width of four times a single particle diameter) while their λ is about 0.064.

4.4. Discussion

Our experimental observations and results highlight a shift in particle focusing behavior between the transition and outlet regions. Accordingly, it is recommended to carefully locate the outlets at the transition region in alternating the curved microchannels, which suggests the potential use of the proposed geometry to separate particles of 15 and 20 μm diameter. Figure 4 illustrates the fluorescent images of the particles' focusing positions in the asymmetric curved microchannel in the transition region. In the current design, the optimum separation of 20 μm from 15 μm particles occurs at $Re \sim 144$. The focusing band of the large particles is apart from that of the medium ones with a distance of approximately 40 μm , which is about twice the diameter of large particles (Figure 4a). As illustrated in Figure 4b, the enrichment of particles with a 20 μm and 10 μm diameter is achieved at $Re \sim 121$ since large particles pass near the centerline while most of the small particles travel between the centerline and W_2 . Similarly, the enrichment of 15 μm and 10 μm particles is obtained at $Re \sim 121$. According to Figure 4c, the stream of medium particles is seen near the centerline while most of the small particles travel between the centerline and W_2 .

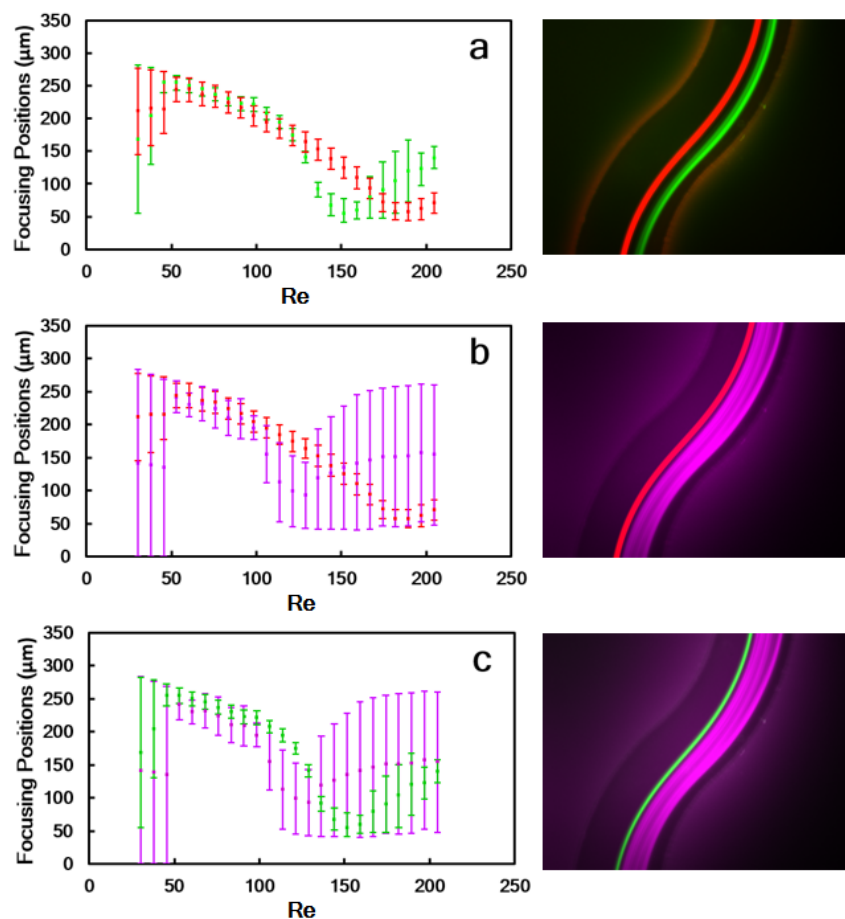


Figure 4. Focusing position of combinations of microparticles of diameter (a) 20 μm and 15 μm , (b) 20 μm and 10 μm , and (c) 15 μm and 10 μm at the transition region versus Reynolds number (left column), and particle streams for optimum separation or enrichment potential at Reynolds numbers of 144, 121 and 121, respectively (right column). Error bars indicate the width of the focusing streak.

Inertial focusing in a symmetric microchannel with the same curvature angle of 280° was previously studied in our group [63]. The focusing behavior of microparticles of the same diameters in an asymmetric microchannel is also compared to that in our previous study. Figure 5 illustrates

the focusing position and width of the microparticles in symmetric and asymmetric microchannels. According to Figure 5a, the 20 μm particles focus as narrower bands closer to W_1 for Reynolds numbers between 53 and 98 in the transition region of the asymmetric microchannel. Although the dimensions of the channel cross section are the same at the transition region of the symmetric and asymmetric channels, the particle focusing band of both the medium and large particles are closer to W_1 at Reynolds numbers between 53 and 98 in the asymmetric microchannel. The force analysis before the transition region assists in explaining this difference. The particle vertical position is assumed to be between the upper zero Dean velocity line and the upper wall, or between the lower zero Dean velocity line and the bottom wall. Hence, at this region, F_S acts on the particle towards the outer wall, while F_D has the opposite direction. Considering a particle traveling along the asymmetric microchannel, F_S is smaller and F_D is larger in the widened regions, as D_h increases and U_f decreases. When the particles are at the upstream location of the transition region, F_S is smaller in the asymmetric channel, compared to the symmetric one. Therefore, it cannot push the particles to the outer wall as much as it does in the symmetric channel. On the other hand, F_D is larger in the asymmetric channel and pushes the particles toward the inner wall stronger than it does in the symmetric channel. Therefore, when the particles reach the transition region, they become closer to W_1 in the asymmetric channel compared to the symmetric one.

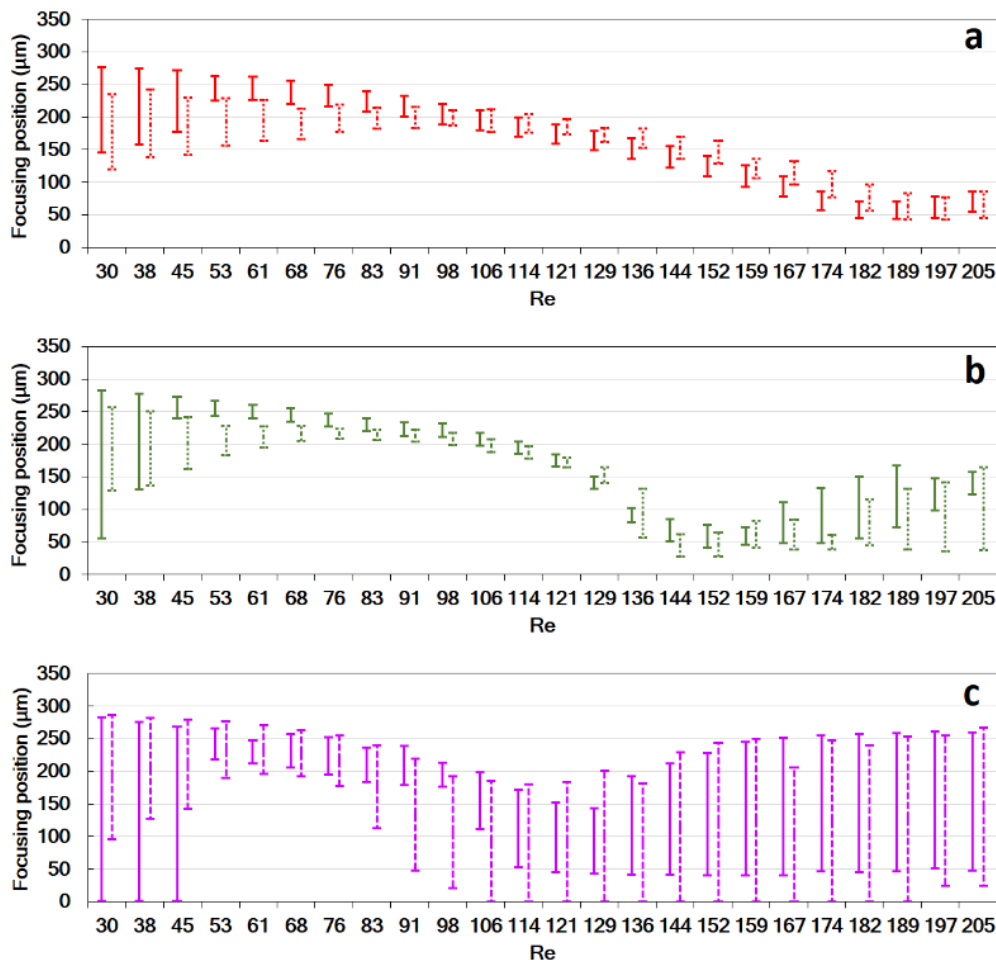


Figure 5. Focusing position against Reynolds numbers for microparticles of (a) 20 μm , (b) 15 μm , and (c) 10 μm diameter in the transition region of asymmetric (solid bars) and symmetric [63] (dashed bars) curvilinear microchannel, both having a curvature angle of 280° . Error bars indicate the width of the focusing streak.

For the Reynolds numbers higher than 136, they focus closer to W_2 in the asymmetric microchannel, while their width is almost identical to that in the symmetric microchannel. Figure 5b corresponds to the 15 μm particles; accordingly, they tend to focus closer to W_1 in the asymmetric microchannel for the Reynolds numbers up to approximately 114. Beyond this Re , there is no consistent pattern in the width and position of the particles' streams. However, the largest distance between the focusing bands of these particles in the symmetric channel is three times that in the asymmetric channel. In other words, the symmetric microchannel exhibits a higher separation potential for the current particles sizes. According to Figure 5c, for all of the Reynolds numbers greater than 53, the focusing band of the small particles is smaller in the asymmetric microchannel than that in the symmetric one. This difference is more noticeable for the range of 83–129 of Re , for which it becomes narrower by a factor of at least two. When the vertical position of the particles is between the two zero Dean velocity lines, both F_S and F_D act on particles towards the outer wall. As a result of the lack of a balancing force, the particles are defocused in this region. Therefore, they approach the centerline in the vertical direction because of the reduced vertical component of F_S . This is because an increase in the flow velocity leads to a smaller C_L . This effect is amplified by reducing the particle size. When the small particles are at the upstream of the transition section, D_h is larger and U_f is smaller in the asymmetric channel than they are in the symmetric one. Hence, up to a certain point, the vertical position of the small particles is assumed to be between the upper zero Dean velocity line and the upper wall or between the lower zero Dean velocity line and the bottom wall in the asymmetric channel, where F_S and F_D balance each other and preserve the particle focusing. If the vertical position of the small particles is assumed to be between zero dean velocity lines, where the directions of both F_S and F_D are towards the outer wall, defocusing occurs. Furthermore, there is an approximately 50 μm distance between the focusing band and the wall of the asymmetric channel, which is not observed in the symmetric geometry, and contrasts with the previous lower limit of 0.07 for λ/D_h for successful focusing to occur.

5. Conclusions

In this study, the focusing behavior of microparticles of 10, 15, and 20 μm diameter in an asymmetric curvilinear microchannel was experimentally investigated. The major conclusions are as follows:

- The focusing of large particles occurred in the transition region over a band having a width of approximately 1.5 times the diameter of a single particle for the Reynolds numbers between 106 and 205, while the focusing width was at least six times that value in the outlet region over the same Re range.
- Medium particles covered a band having a width of 1.5 times the diameter of a single particle in the transition region for Re range of 61–136. They focused in a line as wide as the diameter of a single particle for Re values between 76 and 167 in the outlet region.
- The minimum width of the focusing band of the small particles in the transition region was 3.6 times the diameter of a single particle at Re of 98. This value for the outlet region was at least ten times the diameter of a single particle.
- The focusing behavior of the small particles in the proposed asymmetric microchannel significantly differs from that in the symmetric channel. The dissimilarities include narrower focusing band and noticeable distance from the wall W_2 in the asymmetric microchannel.
- Placing the outlets at the transition region implies the potential use of the proposed geometry in particle or cell separation applications. At Re of 121, the streams of the large and small particles were separated by the largest distance, similar to the medium and small particles. The separation of the large and medium particles was obtained at Re of 144, with a distance of around two times the diameter of large particles.

Author Contributions: Conceptualization, A.K., A.Ö., and M.K.; data curation, A.Ö. and M.K.; formal analysis, A.K., A.Ö., and M.K.; funding acquisition, A.K.; investigation, A.Ö. and M.K.; methodology, A.Ö. and M.K.; project administration: A.K., A.Ö., and M.K.; supervision, A.K.; validation, A.K., A.Ö., and M.K.; visualization, A.Ö., M.K., and H.A.; writing (original draft preparation), A.Ö.; writing (review and editing), A.K., A.Ö., M.K., and H.A.

Funding: This work was supported by the Sabanci University Internal Research Grant, No. IACF15-1444; the Science Academy Outstanding Young Investigator Support Program (BAGEP); the Turkish Academy of Science (TUBA); and the Outstanding Young Investigator Support Program (GEBIP).

Acknowledgments: The authors would like to thank Dr. Batu Erman from the Molecular Biology, Genetics, and Bioengineering Program at Sabanci University for the scientifically-rich consultations. The authors utilized the experimental devices of Sabanci University SUNUM Nanotechnology Research Center and Faculty of Engineering and Natural Sciences (FENS) of Sabanci University.

Conflicts of Interest: The authors declare no conflict of interest.

References

- Oda, R.P.; Strausbauch, M.A.; Huhmer, A.F.R.; Borson, N.; Jurens, S.R.; Craighead, J.; Wettstein, P.J.; Eckloff, B.; Kline, B.; Landers, J.P. Infrared-mediated thermocycling for ultrafast polymerase chain reaction amplification of DNA. *Anal. Chem.* **1998**, *70*, 4361–4368. [[CrossRef](#)] [[PubMed](#)]
- Wilding, P.; Shoffner, M.A.; Kricka, L.J. PCR in a silicon microstructure. *Clin. Chem.* **1994**, *40*, 1815–1818. [[PubMed](#)]
- Burns, M.A.; Johnson, B.N.; Brahmasandra, S.N.; Kalyan, H.; James, R.W.; Madhavi, K.; Timothy, S.S. An integrated nanoliter DNA analysis device. *Science* **1998**, *282*, 484–487. [[CrossRef](#)] [[PubMed](#)]
- Altendorf, E.; Zebert, D.; Holl, M.; Vannelli, A.; Wu, C.; Schulte, T. Results obtained using a prototype microfluidics-based hematology analyzer. In *Micro Total Analysis Systems*; Springer: Dordrecht, The Netherlands, 1998; pp. 73–76.
- Fu, A.; Spence, C.; Scherer, A.; Arnold, F. A microfabricated fluorescence-activated cell sorter. *Nat. Biotechnol.* **1999**, *17*, 1109–1111. [[CrossRef](#)] [[PubMed](#)]
- Knight, J.B.; Vishwanath, A.; Brody, J.P.; Austin, R.H.; Manz, A. Hydrodynamic Focusing on a Silicon Chip: Mixing Nanoliters in Microseconds. *Phys. Rev. Lett.* **1998**, *80*, 3863–3866. [[CrossRef](#)]
- Eijkel, J.C.; Prak, A.; Cowen, S.; Craston, D.H.; Manz, A. Micromachined heated chemical reactor for pre-column derivatisation. *J. Chromatogr. A* **1998**, *815*, 265–271. [[CrossRef](#)]
- Lee, W.C.; Bhagat, A.A.S.; Huang, S.; Van Vliet, K.J.; Han, J.; Lim, C.T. High-throughput cell cycle synchronization using inertial forces in spiral microchannels. *Lab Chip* **2011**, *11*, 1359–1367. [[CrossRef](#)] [[PubMed](#)]
- DApolito, R.; Bochicchio, S.; Dalmoro, A.; Angela Barba, A.; Guido, S.; Tomaiuolo, G. Microfluidic investigation of the effect of liposome surface charge on drug delivery in microcirculation. *Curr. Drug Deliv.* **2017**, *14*, 231–238.
- Lee, M.G.; Choi, S.; Kim, H.-J.; Lim, H.K.; Kim, J.-H.; Huh, N.; Park, J.-K. Inertial blood plasma separation in a contraction-expansion array microchannel. *Appl. Phys. Lett.* **2011**, *98*, 253702. [[CrossRef](#)]
- Li, D. *Encyclopedia of Microfluidics and Nanofluidics*; Springer: Boston, MA, USA, 2008.
- Jacobson, S.C.; Hergenroder, R.; Moore, A.W.J.; Ramsey, J.M. Precolumn reactions with electrophoretic analysis integrated on a microchip. *Anal. Chem.* **1994**, *66*, 4127–4132. [[CrossRef](#)]
- Tabeling, P. *Introduction to Microfluidics*; Oxford University Press: New York, NY, USA, 2005.
- Autebert, J.; Coudert, B.; Bidard, F.; Pierga, J.; Descroix, S.; Malaquin, L.; Viovy, J. Microfluidic: An innovative tool for efficient cell sorting. *Methods* **2012**, *57*, 297–307. [[CrossRef](#)] [[PubMed](#)]
- Bhagat, A.A.S.; Bow, H.; Hou, H.W.; Tan, S.J.; Han, J.; Lim, C.T. Microfluidics for cell separation. *Med. Biol. Eng. Comput.* **2010**, *48*, 999–1014. [[CrossRef](#)] [[PubMed](#)]
- Arifin, D.R.; Yeo, L.Y.; Friend, J.R. Microfluidic blood plasma separation via bulk electrohydrodynamic flows. *Biomicrofluidics* **2007**, *1*, 14103. [[CrossRef](#)] [[PubMed](#)]
- Shi, J.; Huang, H.; Stratton, Z.; Huang, Y.; Huang, T.J. Continuous particle separation in a microfluidic channel via standing surface acoustic waves (SSAW). *Lab Chip* **2009**, *9*, 3354–3359. [[CrossRef](#)] [[PubMed](#)]
- Hejazian, M.; Li, W.; Nguyen, N.-T. Lab on a chip for continuous-flow magnetic cell separation. *Lab Chip* **2015**, *15*, 959–970. [[CrossRef](#)] [[PubMed](#)]

19. Jubery, T.Z.; Srivastava, S.K.; Dutta, P. Dielectrophoretic separation of bioparticles in microdevices: A review. *Electrophoresis* **2014**, *35*, 691–713. [[CrossRef](#)] [[PubMed](#)]
20. Mulvana, H.; Cochran, S.; Hill, M. Ultrasound assisted particle and cell manipulation on-chip. *Adv. Drug Deliv. Rev.* **2013**, *65*, 1600–1610. [[CrossRef](#)] [[PubMed](#)]
21. Pratt, E.D.; Huang, C.; Hawkins, B.G.; Gleghorn, J.P.; Kirby, B.J. Rare cell capture in microfluidic devices. *Chem. Eng. Sci.* **2011**, *66*, 1508–1522. [[CrossRef](#)] [[PubMed](#)]
22. Yamada, M.; Nakashima, M.; Seki, M. Pinched flow fractionation: continuous size separation of particles utilizing a laminar flow profile in a pinched microchannel. *Anal. Chem.* **2004**, *76*, 5465–5471. [[CrossRef](#)] [[PubMed](#)]
23. Wu, Z.; Willing, B.; Bjerketorp, J.; Jansson, J.K.; Hjort, K. Soft inertial microfluidics for high throughput separation of bacteria from human blood cells. *Lab Chip* **2009**, *9*, 1193. [[CrossRef](#)] [[PubMed](#)]
24. Liu, Z.; Huang, F.; Du, J.; Shu, W.; Feng, H.; Xu, X.; Chen, Y. Rapid isolation of cancer cells using microfluidic deterministic lateral displacement structure. *Biomicrofluidics* **2013**, *7*, 11801. [[CrossRef](#)] [[PubMed](#)]
25. Hyun, K.-A.; Kwon, K.; Han, H.; Kim, S.-I.; Jung, H.-I. Microfluidic flow fractionation device for label-free isolation of circulating tumor cells (CTCs) from breast cancer patients. *Biosens. Bioelectron.* **2013**, *40*, 206–212. [[CrossRef](#)] [[PubMed](#)]
26. Preira, P.; Grandne, V.; Forel, J.-M.; Gabriele, S.; Camara, M.; Theodoly, O. Passive circulating cell sorting by deformability using a microfluidic gradual filter. *Lab Chip* **2013**, *13*, 161–170. [[CrossRef](#)] [[PubMed](#)]
27. Ji, H.M.; Samper, V.; Chen, Y.; Heng, C.K.; Lim, T.M.; Yobas, L. Silicon-based microfilters for whole blood cell separation. *Biomed. Microdevices* **2008**, *10*, 251–257. [[CrossRef](#)] [[PubMed](#)]
28. Yamada, M.; Kano, K.; Tsuda, Y.; Kobayashi, J.; Yamato, M.; Seki, M.; Okano, T. Microfluidic devices for size-dependent separation of liver cells. *Biomed. Microdevices* **2007**, *9*, 637–645. [[CrossRef](#)] [[PubMed](#)]
29. Bhagat, A.A.S.; Kuntaegowdanahalli, S.S.; Papautsky, I. Enhanced particle filtration in straight microchannels using shear-modulated inertial migration. *Phys. Fluids* **2008**, *20*, 101702. [[CrossRef](#)]
30. Liu, C.; Hu, G.; Jiang, X.; Sun, J. Inertial focusing of spherical particles in rectangular microchannels over a wide range of Reynolds numbers. *Lab Chip* **2015**, *15*, 1168–1177. [[CrossRef](#)] [[PubMed](#)]
31. Wang, X.; Zandi, M.; Ho, C.-C.; Kaval, N.; Papautsky, I. Single stream inertial focusing in a straight microchannel. *Lab Chip* **2015**, *15*, 1812–1821. [[CrossRef](#)] [[PubMed](#)]
32. Kim, Y.W.; Yoo, J.Y. The lateral migration of neutrally-buoyant spheres transported through square microchannels. *J. Micromech. Microeng.* **2008**, *18*, 065015. [[CrossRef](#)]
33. Chun, B.; Ladd, A.J.C. Inertial migration of neutrally buoyant particles in a square duct: An investigation of multiple equilibrium positions. *Phys. Fluids* **2006**, *18*, 031704. [[CrossRef](#)]
34. Bhagat, A.A.S.; Kuntaegowdanahalli, S.S.; Papautsky, I. Inertial microfluidics for continuous particle filtration and extraction. *Microfluid. Nanofluid.* **2009**, *7*, 217–226. [[CrossRef](#)]
35. Zhou, J.; Papautsky, I. Fundamentals of inertial focusing in microchannels. *Lab Chip* **2013**, *13*, 1121. [[CrossRef](#)] [[PubMed](#)]
36. Hur, S.C.; Brinckerhoff, T.Z.; Walthers, C.M.; Dunn, J.C.Y.; Di Carlo, D. Label-Free Enrichment of Adrenal Cortical Progenitor Cells Using Inertial Microfluidics. *PLoS ONE* **2012**, *7*, e46550. [[CrossRef](#)] [[PubMed](#)]
37. Mach, A.J.; Di Carlo, D. Continuous scalable blood filtration device using inertial microfluidics. *Biotechnol. Bioeng.* **2010**, *107*, 302–311. [[CrossRef](#)] [[PubMed](#)]
38. Zhang, J.; Li, M.; Li, W.H.; Alici, G. Inertial focusing in a straight channel with asymmetrical expansion–contraction cavity arrays using two secondary flows. *J. Micromech. Microeng.* **2013**, *23*, 85023. [[CrossRef](#)]
39. Lee, M.G.; Choi, S.; Park, J.-K. Inertial separation in a contraction–expansion array microchannel. *J. Chromatogr. A* **2011**, *1218*, 4138–4143. [[CrossRef](#)] [[PubMed](#)]
40. Warkiani, M.E.; Tay, A.K.P.; Khoo, B.L.; Xiaofeng, X.; Han, J.; Lim, C.T. Malaria detection using inertial microfluidics. *Lab Chip* **2015**, *15*, 1101–1109. [[CrossRef](#)] [[PubMed](#)]
41. Bhagat, A.A.S.; Hou, H.W.; Li, L.D.; Lim, C.T.; Han, J. Pinched flow coupled shear-modulated inertial microfluidics for high-throughput rare blood cell separation. *Lab Chip* **2011**, *11*, 1870–1878. [[CrossRef](#)] [[PubMed](#)]
42. Lee, M.G.; Shin, J.H.; Bae, C.Y.; Choi, S.; Park, J.-K. Label-Free Cancer Cell Separation from Human Whole Blood Using Inertial Microfluidics at Low Shear Stress. *Anal. Chem.* **2013**, *85*, 6213–6218. [[CrossRef](#)] [[PubMed](#)]

43. Park, J.-S.; Song, S.-H.; Jung, H.-I. Continuous focusing of microparticles using inertial lift force and vorticity via multi-orifice microfluidic channels. *Lab Chip* **2009**, *9*, 939–948. [[CrossRef](#)] [[PubMed](#)]
44. Bhagat, A.A.S.; Kuntaegowdanahalli, S.S.; Dionysiou, D.D.; Papautsky, I. Spiral microfluidic nanoparticle separators. *Proc. SPIE* **2008**, *6886*. [[CrossRef](#)]
45. Martel, J.M.; Toner, M. Inertial focusing dynamics in spiral microchannels. *Phys. Fluids* **2012**, *24*, 032001. [[CrossRef](#)] [[PubMed](#)]
46. Guan, G.; Wu, L.; Bhagat, A.; Li, Z.; Chen, P.; Chao, S. Spiral microchannel with rectangular and trapezoidal cross-sections for size based particle separation. *Sci. Rep.* **2013**, *3*, 1475. [[CrossRef](#)] [[PubMed](#)]
47. Bhagat, A.A.S.; Kuntaegowdanahalli, S.S.; Papautsky, I. Continuous particle separation in spiral microchannels using dean flows and differential migration. *Lab Chip* **2008**, *8*, 1906. [[CrossRef](#)] [[PubMed](#)]
48. Warkiani, M.E.; Guan, G.; Luan, K.B.; Lee, W.C.; Bhagat, A.A.S.; Kant Chaudhuri, P.; Tan, D.S.-W.; Lim, W.T.; Lee, S.C.; Chen, P.C.Y.; et al. Slanted spiral microfluidics for the ultra-fast, label-free isolation of circulating tumor cells. *Lab Chip* **2014**, *14*, 128–137. [[CrossRef](#)] [[PubMed](#)]
49. Warkiani, M.E.; Khoo, B.L.; Tan, D.S.-W.; Bhagat, A.A.S.; Lim, W.-T.; Yap, Y.S.; Lee, S.C.; Soo, R.A.; Han, J.; Lim, C.T. An ultra-high-throughput spiral microfluidic biochip for the enrichment of circulating tumor cells. *Analyst* **2014**, *139*, 3245. [[CrossRef](#)] [[PubMed](#)]
50. Kuntaegowdanahalli, S.S.; Bhagat, A.A.S.; Kumar, G.; Papautsky, I. Inertial microfluidics for continuous particle separation in spiral microchannels. *Lab Chip* **2009**, *9*, 2973. [[CrossRef](#)] [[PubMed](#)]
51. Bhagat, A.A.S.; Kuntaegowdanahalli, S.S.; Kaval, N.; Seliskar, C.J.; Papautsky, I. Inertial microfluidics for sheath-less high-throughput flow cytometry. *Biomed. Microdevices* **2010**, *12*, 187–195. [[CrossRef](#)] [[PubMed](#)]
52. Zhang, J.; Yan, S.; Li, W.; Alici, G.; Nguyen, N.-T. High throughput extraction of plasma using a secondary flow-aided inertial microfluidic device. *RSC Adv.* **2014**, *4*, 33149–33159. [[CrossRef](#)]
53. Li, W.; Yan, S.; Sluyter, R.; Nguyen, N. Inertial particle separation by differential equilibrium positions in a symmetrical serpentine micro-channel. *Sci. Rep.* **2014**, *4*, 4527.
54. Zhang, J.; Li, W.; Li, M.; Alici, G.; Nguyen, N.-T. Particle inertial focusing and its mechanism in a serpentine microchannel. *Microfluid. Nanofluid.* **2014**, *17*, 305–316. [[CrossRef](#)]
55. Zhu, J.; Canter, R.C.; Keten, G.; Vedantam, P.; Tzeng, T.-R.J.; Xuan, X. Continuous-flow particle and cell separations in a serpentine microchannel via curvature-induced dielectrophoresis. *Microfluid. Nanofluid.* **2011**, *11*, 743–752. [[CrossRef](#)]
56. Leighton, D.; Acrivos, A. The shear-induced migration of particles in concentrated suspensions. *J. Fluid Mech.* **1987**, *181*, 415–439. [[CrossRef](#)]
57. Han, M.; Kim, C.; Kim, M.; Lee, S. Particle migration in tube flow of suspensions. *J. Rheol.* **1999**, *43*, 1157–1174. [[CrossRef](#)]
58. Jiang, D.; Tang, W.; Xiang, N.; Ni, Z. Numerical simulation of particle focusing in a symmetrical serpentine microchannel. *RSC Adv.* **2016**, *6*, 57647–57657. [[CrossRef](#)]
59. Amini, H.; Lee, W.; Di Carlo, D. Inertial microfluidic physics. *Lab Chip* **2014**, *14*, 2739. [[CrossRef](#)] [[PubMed](#)]
60. Zhang, J.; Yan, S.; Yuan, D.; Alici, G.; Nguyen, N.-T.; Ebrahimi Warkiani, M.; Li, W. Fundamentals and Applications of Inertial Microfluidics: A Review. *Lab Chip* **2016**, *16*, 10–34. [[CrossRef](#)] [[PubMed](#)]
61. Di Carlo, D. Inertial microfluidics. *Lab Chip* **2009**, *9*, 3038–3046. [[CrossRef](#)] [[PubMed](#)]
62. Di Carlo, D.; Irimia, D.; Tompkins, R.G.; Toner, M. Continuous inertial focusing, ordering, and separation of particles in microchannels. *Proc. Natl. Acad. Sci. USA* **2007**, *104*, 18892–18899. [[CrossRef](#)] [[PubMed](#)]
63. Özbey, A.; Karimzadehkhoei, M.; Akgönül, S.; Gozuacik, D.; Koşar, A. Inertial Focusing of Microparticles in Curvilinear Microchannels. *Sci. Rep.* **2016**, *6*, 38809. [[CrossRef](#)] [[PubMed](#)]
64. Di Carlo, D.; Edd, J.F.; Irimia, D.; Tompkins, R.G.A.; Toner, M. Equilibrium Separation and Filtration of Particles Using Differential Inertial Focusing. *Anal. Chem.* **2008**, *80*, 2204–2211. [[CrossRef](#)] [[PubMed](#)]
65. Gossett, D.R.; Di Carlo, D. Particle Focusing Mechanisms in Curving Confined Flows. *Anal. Chem.* **2009**, *81*, 8459–8465. [[CrossRef](#)] [[PubMed](#)]
66. Vasseur, P.; Cox, R.G.; Feng, J.; Joseph, D.D. The lateral migration of spherical particles sedimenting in a stagnant bounded fluid. *J. Fluid Mech.* **1977**, *80*, 561. [[CrossRef](#)]
67. Matas, J.; Morris, J.; Guazzelli, E. Lateral Forces on a Sphere. *Oil Gas Sci. Technol.* **2004**, *59*, 59–70. [[CrossRef](#)]
68. Martel, J.M.; Toner, M. Inertial Focusing in Microfluidics. *Annu. Rev. Biomed. Eng.* **2014**, *16*, 371–396. [[CrossRef](#)] [[PubMed](#)]

69. Di Carlo, D.; Edd, J.F.; Humphry, K.J.; Stone, H.A.; Toner, M. Particle Segregation and Dynamics in Confined Flows. *Phys. Rev. Lett.* **2009**, *102*, 094503. [[CrossRef](#)] [[PubMed](#)]
70. Zeng, L.; Balachandar, S. Wall-induced forces on a rigid sphere at finite Reynolds number. *J. Fluid Mech.* **2005**, *536*, 1–25. [[CrossRef](#)]
71. Takemura, F.; Magnaudet, J. The transverse force on clean and contaminated bubbles rising near a vertical wall at moderate Reynolds number. *J. Fluid Mech.* **2003**, *495*, 235–253. [[CrossRef](#)]
72. Asmolov, E. The inertial lift on a spherical particle in a plane Poiseuille flow at large channel Reynolds number. *J. Fluid Mech.* **1999**, *381*, 63–87. [[CrossRef](#)]
73. Özbey, A.; Karimzadehkhoei, M.; Bayrak, Ö.; Koşar, A. Inertial focusing of microparticles in curvilinear microchannels with different curvature angles. *Microfluid. Nanofluid.* **2018**, *22*, 62. [[CrossRef](#)]
74. Martel, J.; Toner, M. Particle focusing in curved microfluidic channels. *Sci. Rep.* **2013**, *3*, 3340. [[CrossRef](#)]



© 2018 by the authors. Licensee MDPI, Basel, Switzerland. This article is an open access article distributed under the terms and conditions of the Creative Commons Attribution (CC BY) license (<http://creativecommons.org/licenses/by/4.0/>).